Coherent interdecadal cycles in global rainfall, temperature, and cloud cover

BACKGROUND

Cycles within interdecadal variability are a persistent and widely reported feature in the climate system[1–3]. A central unresolved question is whether this variability represents quasi-periodic cycles arising predominantly from internally generated stochastic fluctuations[1,4,5] or whether these are persistent cycles that display period and amplitude modulation due to weak coupling to external influences[6–8].

Previous studies on interdecadal periodicity have focussed analysis either on limited geographical regions for individual climate variables such as temperature[9,10] and rainfall[2,11]; averaged global datasets[6,12]; or used composite indices like the climate modes[8,13]. While these approaches have provided valuable insights, they each apply some degree of spatial limitation or aggregation. This can obscure variability when phase relationships differ across regions, and therefore provide only a partial view of the global climate system. Recent studies have revealed statistically significant Global Rainfall Cycles of 12.9 and 19.9 years which cannot be accounted for by the dominant climate modes such as the El Niño–Southern Oscillation (ENSO) and the Pacific Decadal Oscillation (PDO)[14,15].

This study aims to address some of these knowledge gaps and limitations by looking at multiple primary climate variables (temperature, rainfall and cloud cover) with full global gridded coverage over the last century. The Gaussian clustering of wavelet average power spectra (GC-WAPS) method enables the aggregation of subtle cyclic signals across extensive spatial networks of climate records, providing enhanced discrimination from red-noise variability to individual site based analysis[14]. We also test the spatial coherence and phase stability of these cycles and present a testable hypothesis leading to practical applications.

METHODS

For signal decomposition analysis, the time series for each grid point was converted to annual values (rainfall sum, temperature and cloud cover mean) and detrended using a linear least-squares fit. The GC-WAPS[14] method was used to identify the dominant cycles at each site:

- Run continuous wavelet transform (Morlet), over full time series, 0.1-yr steps
- Generate global mean power spectrum and automatically select peaks
- Aggregate all peaks and run a Gaussian Mixture Model to find clusters
- Generate AR(1) red noise from individual site data and repeat analysis
- Run standard t-test comparing central tendency of each cluster to red-noise

For spatial coherence maps, all time series were detrended. At each grid point the significant cycles identified in GC-WAPS were extracted from the wavelet transform and also generated as perfect sine waves. The Pearson correlation coefficient (R) was calculated between the time series anomaly and both the wavelet and sine wave. The phase of each sine wave was fixed to the mean at significant sites. Scan QR code below for full methods.

REFERENCES

[1] Liu, Z. Journal of Climate 25, 1963–1995 (2012). [2] Williams, A.P., Anchukaitis, K.J., Woodhouse, C.A., et al. Water Resources Research 57, e2020WR028599 (2021). [3] Scafetta, N. Clim Dyn 43, 175–192 (2014). [4] Power, S. & Colman, R. Climate Dynamics 26 (2006). [5] Latif, M. & Keenlyside, N.S. Deep Sea Research Part II: Topical Studies in Oceanography 58, 1880–1894 (2011). [6] Scafetta, N. Journal of Atmospheric and Solar-Terrestrial Physics 72, 951–970 (2010). [7] Currie, R.G. Journal of Geophysical Research: Atmospheres 89, 1295–1308 (1984). [8] Le Mouël, J.-L., Lopes, F., & Courtillot, V. Journal of Geophysical Research: Atmospheres 124, 2600–2619 (2019). [9] Joshi, M., Hall, R.A., Stevens, D.P., et al. Earth System Dynamics 14, 443–455 (2023). [10] Keeling, C.D. & Whorf, T.P. Proceedings of the National Academy of Sciences 94, 8321–8328 (1997). [11] Chowdhury, P., Gokhale, M.H., Singh, J., et al. Astrophys Space Sci 361, 54 (2016). [12] Ogurtsov, M.G. Geomagn. Aeron. 60, 391–395 (2020). [13] Yasuda, I. Geophysical Research Letters 36, L05605 (2009). [14] Selkirk, T.F., Western, A.W., & Webb, J.A. Hydrology and Earth System Sciences 29, 2167–2184 (2025). [15] Selkirk, T.F., Western, A.W., & Webb, J.A. Hydrology and Earth System Sciences 29, 5737–5754 (2025). [16] Cionco, R.G. & Pavlov, D., PANGAEA (2017); https://doi.org/10.1594/PANGAEA.882534. [17] Carrillo-Sánchez, J.D., Gómez-Martín, J.C., Bones, D.L., et al. Icarus 335, 113395 (2020). [18] Plane, J.M.C. Chem. Soc. Rev. 41, 6507–6518 (2012). [19] Schneider, J., Weigel, R., Klimach, T., et al. Atmospheric Chemistry and Physics 21, 989–1013 (2021). [20] Cziczo, D.J., Froyd, K.D., Hoose, C., et al. Science 340, 1320–1324 (2013).

Tobias F. Selkirk, Andrew W. Western, J.Angus Webb*

Department of Infrastructure Engineering
University of Melbourne, Australia
**tobiasselkirk@gmail.com*

ENVIRONMENTAL RESEARCH
LETTERS

LETTER • **OPEN ACCESS**

Coherent interdecadal cycles in global rainfall, temperature, and cloud cover with alignment to Jovian orbital periods

To cite this article: Tobias F Selkirk *et al* 2026 *Environ. Res. Lett.* **21** 084003

ENVIRONMENTAL RESEARCH
LETTERS

LETTER

Coherent interdecadal cycles in global rainfall, temperature, and cloud cover with alignment to Jovian orbital periods

Tobias F Selkirk*, Andrew W Western and J Angus Webb

Department of Infrastructure Engineering, University of Melbourne, Parkville 3052, Australia
* Author to whom any correspondence should be addressed.

E-mail: selkirkt@unimelb.edu.au

Keywords: rainfall variability, interdecadal climate variability, surface temperature cycles, wavelet spectral analysis, hydroclimate forecasting, interplanetary dust, solar inertial motion

Supplementary material for this article is available online

OPEN ACCESS

RECEIVED
15 December 2025

REVISED
13 March 2026

ACCEPTED FOR PUBLICATION
31 March 2026

PUBLISHED
15 April 2026

Abstract

Interdecadal cycles repeatedly appear in global climate variables such as rainfall, temperature, and the climate modes, yet their origin remains unresolved and is most often attributed either to quasi-periodic artefacts of internal climate variability and red-noise fluctuations, or external lunisolar drivers. Previous studies have often focussed on specific regions, singular variables or aggregated datasets. Here we identify significant coherent 12.9- and 19.9 year cycles in globally gridded datasets of rainfall, surface temperature, and cloud cover across ∼40% of sites using the Gaussian clustering of wavelet amplitude power spectrum method. Regional clusters of positive and negative correlation are largely balanced spatially meaning these cycles represent a redistribution of energy rather than an overall heating or cooling effect. These signals appear to align closely with orbital dynamics of the Jovian planets with a consistent lag of approximately two years. The observed phase, amplitude, and cross-variable consistency suggest a working hypothesis in which gravitational perturbations modulate interplanetary dust influx, potentially driving subtle observed downstream changes in total cloud cover (∼2%), radiative balance (∼0.4 °C), and rainfall (∼10%). These findings empirically suggest that a significant fraction of interdecadal variability may be externally paced, as opposed to arising solely from internal stochastic processes with potential implications for long term rainfall forecasting.

1. Introduction

Cycles within interdecadal variability are a persistent and widely reported feature in the climate system (Liu 2012, Scafetta 2014a, Williams *et al* 2021). A central unresolved question is whether this variability represents quasi-periodic cycles arising predominantly from internally generated stochastic fluctuations (Power and Colman 2006, Latif and Keenlyside 2011, Liu 2012) or whether these are persistent cycles that display period and amplitude modulation due to weak coupling to external influences, such as the ∼11-year sunspot cycle or planetary scale drivers (Currie 1993, Scafetta 2010, Le Mouël *et al* 2019). On longer timescales, the impact of orbital variability is on the Earth's climate is well established through the Milankovitch cycles (Hays *et al* 1976, Lorius *et al* 1985, Jouzel *et al* 2007), however, whether external influences on climate could exist at shorter timescales remains highly controversial (Briffa 1994). Resolving the origins of interdecadal cycles in the climate system could help to distinguish internal variability from externally paced signals and is critical to understanding trends and patterns in the global climate.

The prevailing interpretation is currently that interdecadal variability arises largely through ocean-atmosphere coupling and non-linear feedbacks (Latif and Keenlyside 2011, Liu 2012). Broadly speaking, this variability feeds large-scale climate modes such the El-Nino Southern Oscillation (ENSO) and the Interdecadal Pacific Oscillation (IPO) which in turn modulate a portion of surface temperature, precipitation and circulation patterns (Ghil and Vautard 1991, Cayan *et al* 1998, Allan 2000, An and Wang 2000, Baines 2011). The quasi-periodicity observed is thought to be transient and emergent of red-noise processes rather than phase-stable signals.

There is also a large body of literature which claims that a component of the decadal variability of climate modes is not internally driven but weakly coupled to lunisolar drivers such as the 18.6 year Lunar Nodal Cycle (Yasuda 2018), the ∼22 year Hale magnetic cycle (Le Mouël *et al* 2019) or the ∼11 year Schwabe cycle (Ormaza-González *et al* 2022). The lunar framework typically involves gravitational modulation of oceanic and atmospheric tides driving subtle changes in the climate (Joshi *et al* 2023, Yasuda 2018). In parallel, the solar-planetary line of research proposes a dynamical framework where orbital combinations of the planets could transmit angular momentum and kinetic moments to both solar and terrestrial rotational dynamics (Scafetta 2014b, Lopes *et al* 2021). Other studies have suggested that a more direct influence of the Jovian planets (Jupiter, Saturn, Uranus and Neptune) on terrestrial climate could occur through the modulation of cosmic dust entering the atmosphere (Ogurtsov 2020, Scafetta *et al* 2020). These interpretations continue to be explored, with their applicability at decadal to interdecadal timescales remaining an active area of debate.

Previous studies on interdecadal periodicity have focussed analysis either on limited geographical regions for individual climate variables such as temperature (Joshi *et al* 2023, Keeling and Whorf 1997) and rainfall (Chowdhury and Beecham 2012, Williams *et al* 2021); averaged global datasets (Scafetta 2010, Ogurtsov 2020); or used composite indices like the climate modes (Yasuda 2018, Le Mouël *et al* 2019). While these approaches have provided valuable insights, they each apply some degree of spatial limitation or aggregation. This can obscure variability when phase relationships differ across regions, and therefore provide only a partial view of the global climate system. Since climate variable time series are inherently noisy at higher frequencies, identifying the significance of weak interdecadal signals against a red-noise background using individual spectra can be challenging.

This study aims to address some of these limitations by looking at multiple primary climate variables (temperature, rainfall and cloud cover) with full global gridded coverage over the last century. Wavelet analysis is ideal for identifying periods with amplitude and frequency modulation but is traditionally limited to analysis of a small number of spectra. The Gaussian clustering of wavelet average power spectra (GC-WAPS) method enables the aggregation of subtle cyclic signals across extensive spatial networks of climate records, providing enhanced discrimination from red-noise variability to individual site based analysis (Selkirk *et al* 2025a). We also aim to test the spatial coherence and phase stability of these cycles and to present a testable hypothesis leading to practical applications.

Here we show highly statistically significant ($p < 0.001$) clusters of coherent ∼13- and ∼20 year cycles in detrended rainfall, surface temperature, and total cloud fraction (tcf) across ∼40% of global land areas. The resulting patterns exhibit organised regions of positive and negative phase alignment, forming large-scale teleconnection-like structures rather than isolated local responses. At sites exhibiting significant periodicity, the mean cycle amplitude in total cloud cover change is approximately 2%, corresponding to an observed ∼0.4 °C modulation of surface temperature, closely consistent with the estimated scale of effect derived from longwave cloud radiative effect (LWCRE) sensitivity. The cycles capture an average of 10%–11% of the rainfall variance in significant regions, with the strongest signal being detected in eastern Australia, where the timing aligns with epochs of extended drought. Regions of positive and negative correlation are mostly balanced, meaning these cycles represent a redistribution of rainfall and energy rather than an overall heating or cooling effect.

In total, there were five significant cycles detected in global rainfall. Though cycles above 30 years are treated with some caution due to their length relative to the time series, all five cycles coincide closely (<1%) to the synodic periods of the Jovian planets as measured empirically through solar inertial motion (SIM) with a 2 year lag (table 1). In contrast, correlation to the ∼11 yr and ∼22 year solar magnetic cycles is poor. The observed phase coherence, amplitude, and cross-variable consistency are compatible with a working hypothesis that gravitational perturbations from the Jovian planets may modulate interplanetary dust influx, leading to downstream changes in cloud cover, radiative balance, and rainfall, as recently proposed by other authors (Ogurtsov 2020, Scafetta *et al* 2020). This paper does not claim to resolve the mechanism but provides empirical constraints that may inform avenues for future research to provide a dynamical model.

2. Methods

GPCC Full Data Monthly Product Version 2022 (2.5°) was used for global gridded rainfall analysis from 1890 to 2020 (Schneider *et al* 2022). For temperature, the non-infilledHadCRUT5 global surface temperature anomalies ensemble mean version 5.0.2.0 values from 1850 to 2025 were accessed through the Met Office Hadley Centre & University of East Anglia Climatic Research Unit (Morice *et al* 2021). The total cloud cover ensemble monthly mean from 1806 to 2015 was taken from the NOAA/CIRES/DOE 20th Century Reanalysis (V3) dataset (Slivinski *et al* 2019). Solar barycentre motion was accessed through the PANGEA repository (Cionco and Pavlov 2017) for EPM2017H (Cionco and Pavlov 2018). See *Extended*

Materials and Methods in the supplement for details on dataset preparation and specific methodologies.

To identify interdecadal cycles in each dataset we used the GC-WAPS method, recently developed for detecting significant periodic signals in large sets of time series data (Selkirk *et al* 2025a). GC-WAPS applies a continuous wavelet transform to decompose time series into frequency components and generate a global mean power spectrum (GMPS) by averaging the absolute wavelet coefficients across the time series. All time series were detrended prior to analysis. Incomplete sites were filtered from the temperature and rainfall datasets to avoid artefacts in wavelet analysis from the infilling by climatological normals (see supplementary materials figures S2(a) and S3(a)).

Peaks in the GMPS at each site were automatically selected and aggregated. A Gaussian mixture model (GMM) was then used to identify clusters of periods with a probability distribution density higher than expected compared to randomly generated red noise, as opposed to the power density of a single wavelet spectra. The first order autoregressive AR(1) parameter (α) and standard deviation (SD) (σ) were calculated for each data point time series and used to generate a custom red-noise time series (see supplementary materials for additional details). The wavelet analysis and peak extraction described above were then repeated using the randomly generated data for all data points, followed by GMM clustering, creating a red noise distribution that was inclusive of any potential bias introduced in the signal processing.

For the statistical significance of the clustering, we used a standard t-test to assess the central tendency of each cluster compared to those from red noise. The null hypothesis was that there would be no significant difference in the spread of periods between the two groups, indicating a random distribution of periods across all sites. The residual was calculated by taking the absolute value of subtracting each data point within a cluster from the cluster mean for both the annual variable data (group 1) and randomly generated data (group 2). We adopted a highly conservative type-1 error rate of 0.001, given the size of the data set.

For global spatial coherence and scale of influence, the full datasets were used to quantify the presence and strength of the cycles for each data point. Each time series was detrended, then the significant periods found in GC-WAPS of global rainfall (12.9-, 19.9-, 28.2-, 35.9-, 45.4-year) were extracted from the wavelet transform at each site. A sliding-window Pearson correlation coefficient (R) was computed between the observed signal and a reference cycle (sine wave of matching period) across a range of lags to find the cycle offset. This value was used to generate a stable sine wave.

The Pearson coefficient and associated p-value were then calculated to evaluate cyclicity in three ways: (1) correlation between the extracted wavelet and time series anomalies, providing a direct measure of each cycle's contribution to rainfall, temperature and cloud cover while accounting for frequency and amplitude modulation; (2) correlation between the fixed sine wave (above) and the three climate variable anomalies, indicating the stability of the cycle's influence; and (3) correlation between the fixed sine wave and the extracted wavelet, assessing phase alignment and cycle stability. The null hypothesis was that the distributions are uncorrelated. The coefficient of determination (R^2) was used as the estimate of variance explained by each cycle. Additionally, the signal-to-noise ratio was computed as the peak amplitude of the extracted wavelet divided by the site's SD, providing a measure of cycle amplitude relative to background variability for rainfall.

Phase comparisons were completed by extracting the real component of the 12.9- and 19.9 yr wavelet transform from Nino 3.4 sea-surface temperature (SST) (1870–2025) and the IPO (1871–2016) for ENSO. *EPM2017H A new long-term high-precision ephemeris* (Cionco and Pavlov 2018) was used for SIM and a proxy of combined gravitational influence. Pearson correlations were calculated between the offset SIM and all other variables (climate modes, rainfall, temperature, cloud cover). All wavelets were normalised from -1 to 1 for direct visual comparison.

To estimate the proportional change in surface temperature from the modulation of cloud cover, we used the method outlined by Ogurtsov (2020). The most recent estimate of the surface LWCRE sensitivity, -26.3 ± 3.8 W m^{-2} per percentage-point change in annual-mean tcf (L'Ecuyer *et al* 2019), was used to calculate the amplitude of each cycle. The LWCRE sensitivity was multiplied by the observed fractional amplitude in tcf. For example, for the 12.9 year cycle:

$$\Delta F = \text{LWCRE} \times \%\text{tcf} = 26.3\ \text{Wm}^{-2} \times 0.0211 = 0.5549\ \text{Wm}^{-2}.$$

The IPCC Sixth Assessment Report quotes an effective radiative forcing of 3.93 ± 0.47 W m^{-2} for a doubling of carbon dioxide, along with an equilibrium climate sensitivity of 2.5 °C–4.0 °C, giving a range of 0.64 °C–1.02 °C change per W m^{-2} change in ΔF. For the 12.9 year cycles this results in an estimated average surface temperature change of 0.46 °C (0.35 °C to 0.56 °C). This calculation was repeated for each cycle (12.9-, 19.9-, 29.5-, 35.9 and 45.4 years).

The maximum influence of each planetary alignment combination was estimated from the peak-to-peak amplitude of the extracted wavelet for SIM (supplementary materials tables 1 and 2).

For the illustrative long-term rainfall the first three cycles from SIM (12.9-, 19.9-, and 29.4 years) were extracted from the wavelet transform of the site

annual rainfall and SIM datasets. A 2 year lag was applied to all SIM cycles before combining the three waveforms and calculating the Pearson correlation. The Gamma distribution of rainfall was calculated across the whole time series, as well as separately for all years when the combined SIM cycles were in the negative and positive phase.

3. Results

3.1. Interdecadal cycles in global rainfall, temperature and cloud cover

The GC-WAPS analysis of global rainfall, surface temperature and tcf showed consistent ∼13 and ∼20 year cycles across all three datasets (figure 1). Significant clusters in both the temperature ($\mu =$ 12.5 years, SD 1.0 ; $p < 0.001$) and cloud cover ($\mu =$ 12.7 years, SD 1.0; $p < 0.001$) were observed in close agreement with the 12.9 year Global Rainfall Cycle (GRC) identified previously (Selkirk *et al* 2025b; SD 1.1; $p < 0.001$). The cluster peaks were more distinct in temperature and cloud cover than in rainfall, as reflected by a higher probability distribution density of dominant periods across sites (0.045–0.050 versus 0.035), and a lower SD indicating a sharper and more coherent signal across a broader set of locations. The 12.9 year cycle is close to the mean of the orbital period of Jupiter (11.9 years), and its conjunctions with Neptune (12.8 years) and Uranus (13.8 years). The proximity of those three cycles means they cannot be individually isolated by signal decomposition, but instead present as a continuous ∼12.9 year cycle that shows amplitude and frequency modulation due to wave interference as can be seen from the wavelet extracted from SIM (supplementary materials figure S1(b)).

The 19.9 year GRC also carried through the datasets to both temperature ($\mu =$ 20.2 year, SD 1.2; $p < 0.001$) and cloud cover ($\mu =$ 20.6 year, SD 0.9; $p < 0.001$). This cycle length is also precisely the length between successive heliocentric conjunctions of Jupiter (J) and Saturn (S). The results for the remaining three cycles (∼30, ∼36 and ∼45 years) are less definitive across all three datasets. With clustering observed in the underlying histogram around the similar periodicities, but at a smaller proportion of sites and with lower significance (figure 1). We therefore concentrated analysis on the 12.9- and 19.9 year periods, with full statistics for the longer periods provided in supplementary materials table S2.

All five significant cycles in the GC-WAPS rainfall analysis align closely to the Jovian orbital cycles measured through the SIM proxy with less than 1% error (table 1). The 28.2 year cycle is very close to the 29.4 year orbit of Saturn (S). With the 35.9 year cycle coinciding with the conjunctions of Saturn and Neptune (N), and the 45.4 year cycle with Saturn and Uranus (U) being near perfect. The alignment of all cycles is worth noting, although the 35.9- and 45.4 year cycles were treated with some caution due to their long period relative to the time series length.

Two more cycles appear in the cloud and temperature datasets with greater significance and probability distribution density than for rainfall. A ∼5 year cycle in temperature ($\mu =$ 5.0 year, SD 1.2; $p < 0.001$) and cloud cover ($\mu =$ 5.8 year, SD 1.7; $p < 0.0001$) is close to the 4.1-year cycle ($p > 0.1$) in rainfall assumed to be the quasi-periodic ENSO signal, which has a well-documented oscillation between 2–7 years (Sarachik and Cane 2010). A 350 year reconstruction of SST in the southwest pacific also revealed significant cycles ($p < 0.01$) of 5.7-, 8-, 12- and 19 years, indicating that they are a stable feature over time (DeLong *et al* 2012). ENSO is known to influence global temperature (Allan 2000), but it is notable that the ∼5 year cycle seems more prominent in temperature and cloud cover than rainfall. A ∼9 year cycle was also detected as highly significant in temperature ($\mu =$ 8.8 year, SD 0.9; $p < 0.001$) and cloud cover ($\mu =$ 9.0 year, SD 1.0; $p < 0.001$), though there was not a significant equivalent in rainfall. The ∼20-, ∼9 and ∼5 year cycles in temperature are also consistent with those detected in previous studies using the maximum entropy and the multi-taper methods (Scafetta 2010).

3.2. Global spatial coherence, phase locking and scale of influence

The impact of the 12.9- and 19.9 year cycles is further strengthened by considering the spatial distribution, amplitude and phase alignment across variables. A fixed phase 12.9 year cycle shows a high degree of spatial coherence when correlated with the detrended time series anomalies for rainfall, temperature and cloud cover (figure 2). The dominant offsets for the 12.9- and 19.9 year cycles were consistent across all datasets.

Analyzing the regions where the signal appears stronger, we can see broad agreement between the phase of cloud cover and rainfall for the 12.9 year cycle (figures 2(a) and (c)). Through Australasia and northern Canada, the cycles are positively correlated (red), while central America, Europe and the middle East are in the opposite phase (blue). Over Europe, reduced cloud fraction coincides with higher temperature, consistent with the expected short-wave albedo effect of clouds (Wild *et al* 2017). Cloud–temperature–rainfall interactions depend on cloud type, altitude, and regional circulation and vary on shorter time scales (Li *et al* 2025). Nonetheless, the patterns are broadly consistent with large-scale climate behaviour.

The relationship of the 12.9 year GRC to ENSO is illustrated by lower cloud cover over the Niño 3.4 region of the Pacific Ocean (latitude: −5°

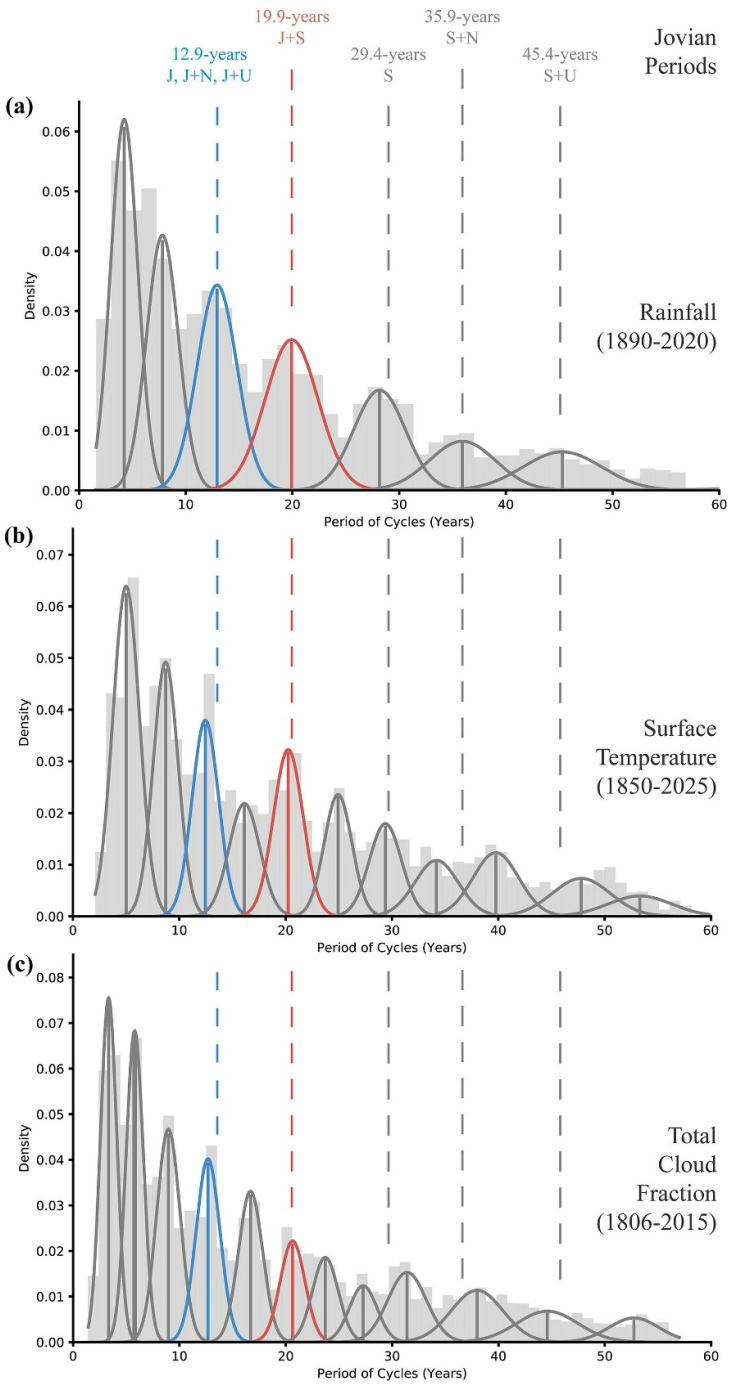

Figure 1. Alignment of interdecadal cycles across three independent datasets by GMM clustering of wavelet analysis and alignment to synodic conjunctions of the Jovian planets. The dark grey histogram represents the total number of sites where each cycle was observed. The *y*-axis represents the probability distribution density of dominant cycle periods across sites and is not a measure of wavelet power or spectral energy. (a) Results of the GC-WAPS analysis of global gauged annual rainfall using the GPCC v2022 gridded (2.5°) dataset, significant clusters ($p < 0.005$) near12.9-, 19.9 years are seen in all three datasets, further significant cycles ($p < 0.05$) at 28.2-, 35.9-, and 45.4-yearsall align in length to the heliocentric conjunction period of the Jovian planets. (b) Results of the GC-WAPS analysis of global surface temperature using the HadCRUT5 (5°) gridded dataset, cycles clustered around 12.5- and 20.2 years are highly significant ($p < 0.001$). (c) Results of the GC-WAPS analysis of global cloud cover using the NOAA-CIRES-DOE 20th Century Reanalysis V3 gridded (2.5°) dataset, with highly significant cycle clusters ($p < 0.001$) at 12.7- and 20.6-years. Significant peaks are identified by testing each cluster against an AR(1) red noise null. See supplementary materials figures S2–S4 for detailed individual analysis.

to 5°, longitude:-170° to −120°) coinciding with lower SST and increased rainfall through Australasia (figures 2(a) and (b)). During La Niña, SST cools in the central Pacific despite increased shortwave radiation, because enhanced upwelling and latent heat loss remove heat from the surface more efficiently than it is gained through solar input (Wang and McPhaden 2000).

The 12.9 year cycle only contributes 11% to the total SST variance in the Niño 3.4 region (supplementary materials figure S1(f)). Hence, while not the primary driver, it appears to be a component of

Table 1. Comparison of the synodic conjunction periods of the Jovian planets with the significant cycles found by GC-WAPS analysis of global gridded rainfall. Percentage error is calculated by the difference in periods over the theoretical Jovian cycle as measured in SIM. The 12.9 year cycle appears as single peak in the mean power spectrum of wavelet analysis as the three periods are too close to individually resolve (see supplementary materials figure S1).

Cycle	Jovian cycle		Length (yr)	GC-WAPS rainfall results (yr)	Difference (yr)	% Error
	Jupiter Orbit (J)	(11.9)				
1	Jupiter & Neptune (JN)	(12.8)	12.9	12.9	0.00	0.00%
	Jupiter & Uranus (JU)	(13.8)				
2	Jupiter & Saturn (JS)		19.9	19.9	0.00	0.00%
3	Saturn Orbit (S)		29.4	28.5	0.90	3.06%
4	Saturn & Neptune (SN)		35.9	35.9	0.00	0.00%
5	Saturn & Uranus (SU)		45.4	45.4	0.00	0.00%
					Mean	**0.61%**

the ENSO system. The peak amplitude of 0.41 °C in the Niño3.4 SST (supplementary materials figure S1(f)), is in close agreement with average temperature observed in the HadCrutt5 dataset (0.42 °C; figure 2(b)). The distributions in figure 2 show a relatively even mixture of positive (red) and negative (blue) correlations globally, indicating that these cycles represent a redistribution of energy rather than an overall heating or cooling effect.

The mean amplitude of the 12.9-year cycle across all filtered sites ($|R| > 0.1$) in the temperature dataset is 0.42 °C (SD 0.2; 95%CI 0.38–0.46 °C, $n = 1{,}065$), and 2.11% (SD 1.1; 95%CI 1.78–2.46 °C, $n = 2{,}423$) for cloud cover. We can estimate the expected average temperature change from the observed variation in cloud cover by using surface the LWCRE sensitivity, -26.3 ± 3.8 W m^{-2} per percentage-point change in annual-mean tcf (Ogurtsov 2020). A variation of 2.11% total cloud cover translates to a change in total radiation forcing (ΔF) of 0.55 W m^{-2} and an average surface temperature change of 0.46 °C (0.35 °C to 0.56 °C), remarkably close to the mean 0.42 °C amplitude observed. Similarly for the 19.9 year cycle, the observed 2.03% amplitude in cloud cover translates to a theoretical 0.41 °C variation in temperature, again very similar to the observed 0.43 °C amplitude (supplementary materials table 1). These two results provide strong support for the scale of influence observed between datasets.

The phase offset was consistent across significant sites in all three climate variables, as well as for 12.9- and 19.9 year cycles extracted from ENSO (Niño 3.4 SST) and the IPO time series (figure 3). Given the strong overlap in GRCs with the orbital and conjunction periods of the Jovian planets, the phase coherence is also considered. SIM is used as an empirical proxy for the time-varying configuration of the Jovian planets, and the wavelets in figure 3 are extracted from Solar barycentre dynamics ephemeris data (Cionco and Pavlov 2018) to represent the timing and phasing of their combined gravitational influence. This was particularly important for the 12.9 year cycle as a means of visualising the combined gravitational effect of the three similar Jovian cycles (11.9-, 12.8- and 13.8 years). The combined waveform, shown in red (figure 3(a)), displays the expected amplitude and frequency modulation, as opposed to the stable 19.9 year cycle of Jupiter and Saturn (figure 3(b)). Both the 12.9- and 19.9 year SIM cycles lead the climate variables by two years.

4. Discussion

4.1. Position relative to existing research

The results presented here directly address the central question posed in the introduction regarding the origin of interdecadal climate variability. The widespread spatial coherence, phase stability, and cross-variable consistency of the detected ∼13- and ∼20 year cycles across rainfall, temperature, and cloud cover are difficult to reconcile with purely stochastic internal variability or transient red-noise processes alone. The findings empirically support an external influence which is coherent across the detrended climate variables.

Given the prior research on solar magnetic influences on climate (Scafetta 2010, Le Mouël *et al* 2019) and the proximity of the periods the ∼11 year Schwabe and ∼22 year Hale magnetic cycles would initially appear to be the most viable drivers. However the correlation of those cycles the 12.9 year ($R = -0.04$, not significant) and 19.9 year ($R = 0.22$, not significant) cycles identified here is very poor, with the difference in period causing them to fall steadily out of phase (supplementary materials figure S9). The absence of alignment suggests the dominant external pacing of the cycles identified in this study is unlikely to operate through solar magnetic variability. This motivates consideration of more direct planetary-scale pathways capable of producing these periods.

4.2. Modulation of interplanetary dust influx

The results are consistent with the working hypothesis that gravitational perturbations caused by the

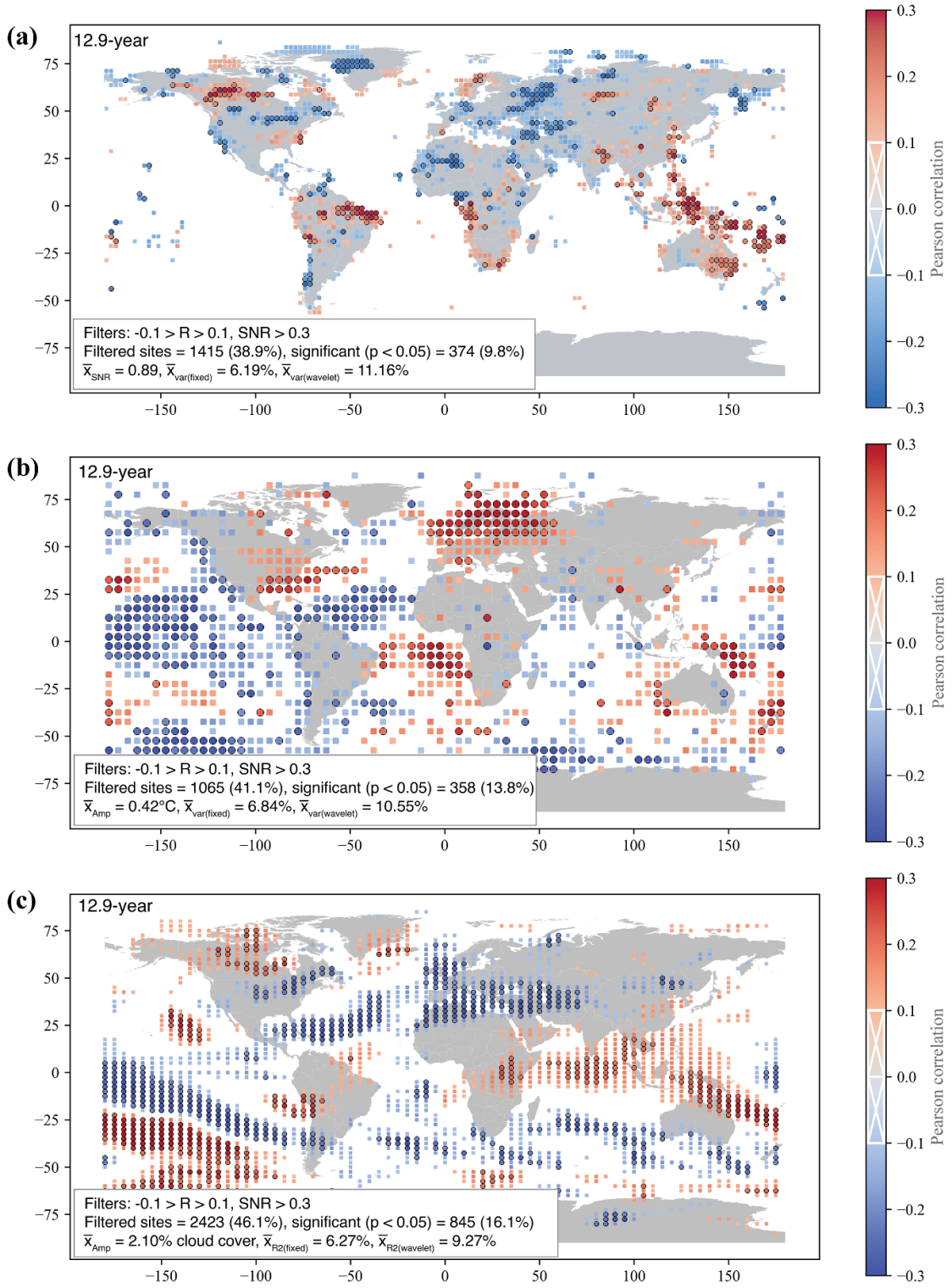

Figure 2. Global distribution of the 12.9 year cycle by Pearson correlation to rainfall, temperature and cloud cover. Grid-points show the Pearson correlation coefficient (R) of a generated 12.9 year sinusoidal signal to the raw anomaly time series of rainfall (a), temperature (b) and cloud cover (c) with significant sites ($p < 0.05$) circled in black. A display threshold of 1% of annual variance is applied. Positive correlation (in phase) is shown in red, with negative correlation (180° out of phase) shown in blue. (a) Reproduced from Selkirk *et al* (2025b). CC BY 4.0.

orbits of the Jovian planets may modulate the influx of interplanetary dust to Earth (Ogurtsov 2020, Scafetta *et al* 2020), the ablation products of which affect cloud dynamics as well as acting as condensation nuclei in the upper atmosphere (Plane 2012), subtly modifying cloud cover, albedo, and downstream rainfall and temperature patterns (figure 4).

Interplanetary dust originates mainly from dust shed by Jupiter-family comets (∼70%) and from continual collisions in the asteroid belt, with smaller

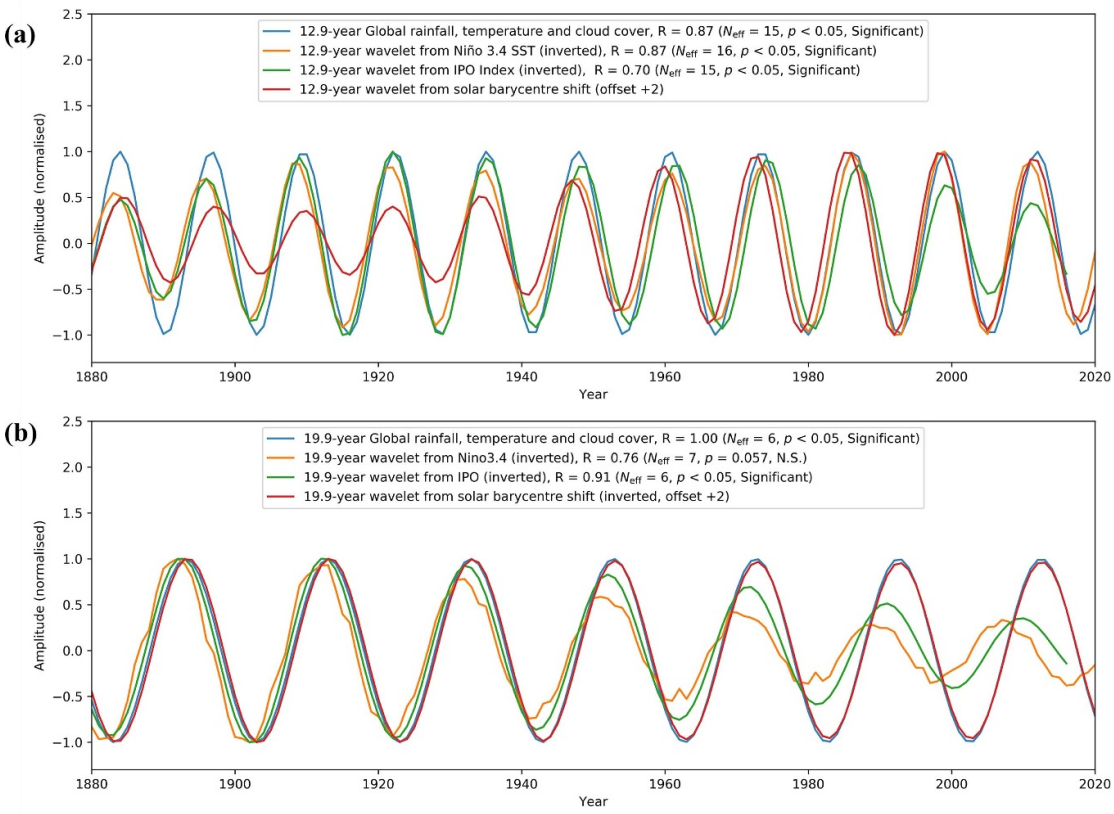

Figure 3. Phase alignment of rainfall, temperature, cloud cover with ENSO and the 12.9 yr and 19.9 year Jovian cycles. Extracted wavelets of the 12.9 year cycle (a) and 19.9 year cycle. (b) show close alignment of the climate variables with ENSO, as well as the same cycles in SIM with a 2 year lag. All waveforms are min-max normalised by peak. The global rainfall, temperature and cloud cover cycles are a generated sine wave with the mean period taken from GC-WAPS distribution and offset taken from the mean of all significant sites. Pearson correlation (R) and significance values are given between the extracted wavelet from the solar barycentre ephemeris (red) and the relevant variable.

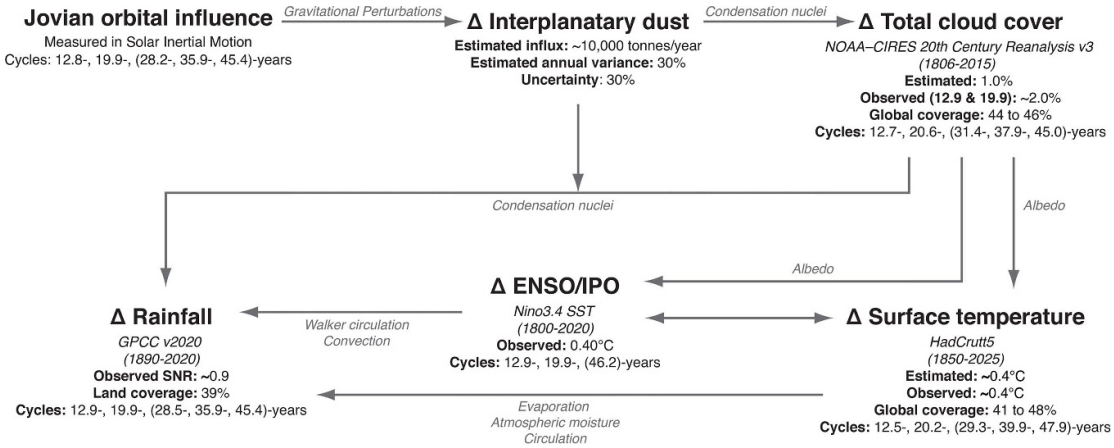

Figure 4. Summary of results and proposed mechanistic pathways for the working hypothesis of gravitational perturbations of Jovian planets on rainfall, temperature and cloud cover via interplanetary dust influx. The range of observed values and coverage are taken from the mean amplitude for 12.9- and 19.9 year cycles in each dataset with sites $R > 0.1$. The interactions between cloud cover, surface temperature, ENSO and rainfall are well established.

contributions from long-period comets, Kuiper Belt objects, and planetary fragments (~30%) (Carrillo-Sánchez *et al* 2020). The range in estimates of total interplanetary dust particle influx to earth is vast: from 1,825 ± 730 t yr^{-1} using high performance radar (Mathews *et al* 2001), to 95 550 t y^{-1}using zodiacal dust cloud observations and modelling (Nesvorný *et al* 2010), with the latest estimates settling around 10 190 ± 3000 t yr^{-1} influx derived from chemical ablation and zodiacal cloud models (Carrillo-Sánchez *et al* 2020). The influence on mesospheric and stratospheric clouds is well established

by *in-situ* and LiDAR studies (Plane 2012). Some authors also claim that interplanetary dust may act as condensation nuclei in the troposphere (Cziczo *et al* 2013, Ogurtsov 2020, Schneider *et al* 2021). While this is disputed, it is well established that the particles trigger a wide range of complex chemical reactions in the mesosphere, stratosphere and troposphere before settling on the earth's surface after rainfall through a process known as wet deposition (Plane 2012).

In-cloud wet deposition may be a form of cloud-nucleus activation, effectively creating a natural seeding of droplets by aerosols, after which the nucleated particles are efficiently scavenged and delivered to the Earth's surface as rainfall (Ogurtsov and Raspopov 2011). The monthly total cloud cover used in this study is column-tcf over the entire model atmosphere, from the surface up to the 20CRv3 model top (∼0.3 hPa) and therefore includes tropospheric and stratospheric clouds (extending into the lower mesosphere) (Slivinski *et al* 2019). The large uncertainty in volume, variance and atmospheric penetration of interplanetary dust makes estimations of potential influence on the troposphere difficult, however consistency of the observed cycles across multiple climate variables provides strong evidence for its climatic influence.

Depending on particle size, the total journey time from the mesosphere to the surface for interplanetary dust can be significant (Plane 2012), taking months to pass through the mesosphere as descent is slowed. An estimated 1–5 years to reach the surface through wet deposition and atmospheric circulation, predominantly through mid latitude tropopause folding (Plane 2012, Dhomse *et al* 2013) is consistent with the 2 year offset observed (figure 3).

Previous authors have estimated that approximately 6.5% of variation in cloud cover may be caused by interplanetary dust, and that a 16% change in dust influx could translate to a change of 1% in cloud cover (Ogurtsov and Raspopov 2011, Ogurtsov 2020). This figure is close to the amplitudes of ∼2% observed in the cloud cover data in this study. The variance is also well within the 29% uncertainty quoted in the latest estimates of dust influx (Carrillo-Sánchez *et al* 2020), or the ∼25% range recorded at the Earth's surface in Antarctica (Rojas *et al* 2021). Though there are currently no peer-reviewed studies or models estimating interannual variance in interplanetary dust influx, measurements in polar ice have showed temporal variations of up to 400% over several thousand years (Brook *et al* 2000). Such variance may reflect changes in the dynamics of interplanetary dust transport and accretion.

The modulation of interplanetary dust influx by the gravitational perturbations of the Jovian planets could also reinforce the effect on rainfall through two complementary pathways: land surface temperature and ENSO via SST (figure 4). The local surface temperature–rainfall relationship can be positive or negative depending on multiple factors including geography, moisture supply and circulation (Held and Soden 2006), as observed in the global distribution maps (figure 2). Similarly, lower SSTs in the Niño 3.4 region of the Pacific Ocean correlate with higher rainfall across Australasia and the central Americas, with global teleconnections simultaneously lowering rainfall in South America and the United States (Becker *et al* 2013). The effects of both pathways are regionally specific and are downstream of the change in cloud cover. Given the stability and predictability of the Jovian orbits, a practical application of this research may be the ability to forecast epochs of elevated and reduced rainfall in strongly affected regions like Australia.

4.3. Testable implications and illustrative projection

The current operational forecast horizon for Australian rainfall is approximately three months (Hossain *et al* 2018). In contrast, the ephemeris data underlying SIM are deterministic and can be computed far into the future. Because the SIM signal is highly correlated with the interdecadal component of rainfall, it raises the possibility of extending predictive skill for the interdecadal rainfall well beyond current seasonal limits.

To illustrate this potential and provide a testable hypothesis, we examine a representative station in the Murray–Darling Basin, which is an agriculturally critical region in Australia where rainfall variability has large economic impacts (Kirby *et al* 2014). The 2 year phase offset and GRCs are consistent across eastern Australia. This example is not a forecast, but an illustration of how phase-aligned SIM cycles could inform testable hypotheses about future interdecadal rainfall conditions. The extracted interdecadal rainfall signal aligns closely with the corresponding SIM component with a two-year lag over the past century ($R = 0.9$), capturing both the phase and amplitude of interdecadal wet–dry transitions (figure 5). Using this empirical relationship, we extend the combined SIM signal forward to estimate the likely timing of upcoming wet and dry phases, which can be tested against observations as new data become available.

Separating all years which fall in the positive and negative phase of the combined SIM cycle and comparing the mean of the gamma distribution for each gives a simple estimate of the influence on rainfall. At this site, mean rainfall in the positive phase is 19% higher on average than in the negative phase. Furthermore, every year of extremely low rainfall (SPI < -2) over the past century has fallen the negative phase of the independently derived combined SIM signal. If the historically observed phase relationship were to persist, the next positive-phase epoch would fall in the late 2020s to mid-2030s, followed by a negative-phase epoch in the 2040s.

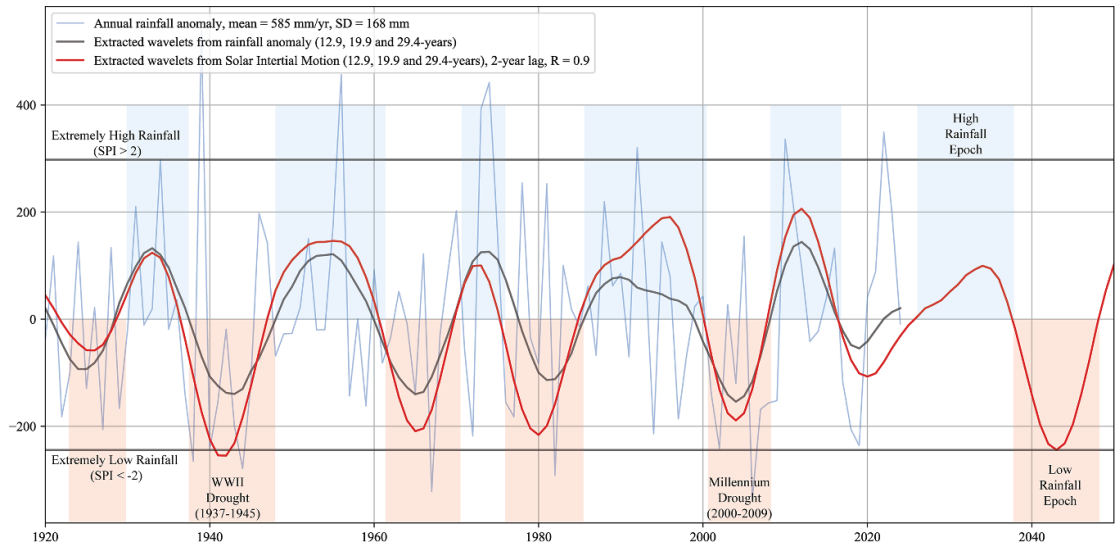

Figure 5. Illustrative long-term rainfall compared to SIM at Rutherglen Research Station (Site 82039) in the Murray–Darling Basin. The grey line shows the 12.9-, 19.9- and 29.4 GRCs extracted from the rainfall anomaly at the site. The red line shows the same cycles extracted from SIM with a 2 year lag. The Pearson correlation between the two independent time series is 0.9. Shaded regions show epochs of high (blue) and low (red) rainfall. Every year of extremely low rainfall (SPI < -2) falls in the negative phase of the SIM cycles.

This is presented solely as a falsifiable expectation derived from the empirical relationship, not as a deterministic forecast. We do not propose that variations in interplanetary dust influx are the sole driver of Australian rainfall. However, the evidence presented here demonstrates a striking and statistically robust relationship between the interdecadal component of Australian rainfall and the gravitationally driven cycles represented in SIM.

From a hydrological perspective, much more rigorous testing would be required to properly quantify the change in relative risk across multiple metrics. From a mechanistic perspective, the next research steps include modelling potential variations in interplanetary dust influx driven by gravitational perturbations from the Jovian planets, simulating the spatial distribution of dust entry into the atmosphere, and examining downstream effects on cloud microphysics and rainfall. Models capable of analysing atmospheric interactions of interplanetary dust the such as Whole Atmosphere Community Climate Model (WACCM) could provide an appropriate framework for testing these hypotheses.

5. Conclusions

This study provides empirical evidence that statistically significant low-frequency signals of ∼13- and ∼20 year periods contribute to interdecadal rainfall, cloud cover and temperature variability across spatially coherent regions at a global scale. The strong period and phase alignment to gravitational perturbations from the Jovian planets informs a working hypothesis that the observed effects may be caused by the modulation of interplanetary dust influx. However, this proposed mechanism is still speculative and would require extensive further research for physical validation. The presence of these cycles in the global climate has practical implications for a deeper understanding of global weather patterns and could ultimately improve the forecasting of interdecadal epochs of flood and drought. Previous authors who have detected similar interdecadal cycles, without identifying their potential origins, have rightfully cautioned against their use in forecasting without a known driver (Williams *et al* 2021). However, the predictability of ephemeris data has allowed us to derive a testable prediction for broad-scale rainfall patterns in significantly affected areas.

At a theoretical level, such predictions can help to inform the range of natural variability in the climate system, which is critical for accurate climate modelling. Recent research on top-of-atmosphere radiative fluxes has suggested that low-cloud feedbacks and decadal variability remain two of the biggest weaknesses in CMIP6-era models (Loeb *et al* 2020). At a conceptual level, these results suggest that Earth's climate is not only shaped by internal variability but could also be also tuned to planetary dynamics, a recognition that could transform both our understanding of natural variability and our capacity to model it.

Acknowledgments

TS was supported by an Australian Government Research Training Program (RTP) Scholarship.

We thank Dr Conrad Wasko (University of Sydney) for his insightful comments and editorial suggestions.

Data availability statement

GPCC Full Data Monthly Product Version 2022 (2.5°) was used for global gridded rainfall analysis available from Deutscher Wetterdienst Website (https://opendata.dwd.de/climate_environment/GPCC/) (Schneider *et al* 2022). The National Oceanic and Atmospheric Administration Physical Science Laboratory landing page (https://psl.noaa.gov/data/) was used to access Niño 3.4 SST Index from the HadISST1.1monthly values from January 1870 to June 2025 (Rayner *et al* 2003)and the total cloud cover ensemble monthly mean from January 1806 to December 2015 from the NOAA/CIRES/DOE 20th Century Reanalysis (V3) dataset (Slivinski *et al* 2019). The Interdecadal Pacific Oscillation 1871–2016 data was accessed through the Ministry for the Environment Data service of the New Zealand Government (https://data.mfe.govt.nz/). Global temperature data were accessed through the Met Office Hadley Centre & University of East Anglia Climatic Research Unit (www.metoffice.gov.uk/hadobs/hadcrut5/data/HadCRUT.5.0.2.0/download.html). The non-infilledHadCRUT5 global surface temperature anomalies ensemble mean version 5.0.2.0 was used (Morice *et al* 2021). Solar barycentre motion was accessed through the PANGEA repository (Cionco and Pavlov 2017) for EPM2017H (Cionco and Pavlov 2018)as tab-delimited text.

No new data were created or analysed in this study.

Extended Methods & Figures available at https://doi.org/10.1088/1748-9326/ae598f/data1.

Code availability

Analyses were performed with standard scientific Python libraries (Python 3.8; NumPy 1.18.1; SciPy 1.4.1; Statsmodels0.11.0; PyWavelets1.1.1; xarray0.20.2; sklearn 0.0.2). The scripts are available from the corresponding author upon request.

Conflict of interest

The authors declare that they have no conflict of interest.

Author contributions

Tobias F Selkirk 0000-0003-3976-4975
Conceptualization (lead), Data curation (lead), Formal analysis (lead), Investigation (lead), Methodology (equal), Validation (equal), Writing – original draft (lead), Writing – review & editing (equal)

Andrew W Western 0000-0003-4982-146X
Conceptualization (supporting), Methodology (supporting), Supervision (equal), Validation (equal), Writing – review & editing (equal)

J Angus Webb 0000-0003-0857-7878
Conceptualization (supporting), Methodology (supporting), Supervision (equal), Validation (equal), Writing – review & editing (equal)

References

Allan R J 2000 ENSO and climatic variability in the past 150 years *El Niño and the Southern Oscillation: Multiscale Variability and Global and Regional Impacts* ed H F Diaz and V Markgraf (Cambridge University Press) pp 3–56 (available at: www.cambridge.org/core/books/el-nino-and-the-southern-oscillation/enso-and-climatic-variability-in-the-past-150-years/D11B615901046601970FF66921BDF431)

An S-I and Wang B 2000 Interdecadal change of the structure of the ENSO mode and its impact on the ENSO frequency* *J. Clim.* **13** 2044–55

Baines P G 2011 Patterns of decadal climate variability and their impact on global rainfall *Proc. Environ. Sci.* **6** 70–87

Becker A, Finger P, Meyer-Christoffer A, Rudolf B, Schamm K, Schneider U and Ziese M 2013 A description of the global land-surface precipitation data products of the global precipitation climatology centre with sample applications including centennial (trend) analysis from 1901–present *Earth Syst. Sci. Data* **5** 71–99

Briffa K R 1994 Grasping at shadows? A selective review of the search for sunspot-related variability in tree rings *The Solar Engine and Its Influence on Terrestrial Atmosphere and Climate* ed E Nesme-Ribes (Springer) pp 417–35

Brook E J, Kurz M D, Curtice J and Cowburn S 2000 Accretion of interplanetary dust in polar ice *Geophys. Res. Lett.* **27** 3145–8

Carrillo-Sánchez J D, Gómez-Martín J C, Bones D L, Nesvorný D, Pokorný P, Benna M, Flynn G J and Plane J M C 2020 Cosmic dust fluxes in the atmospheres of Earth, Mars, and Venus *Icarus* **335** 113395

Cayan D R, Dettinger M D, Diaz H F and Graham N E 1998 Decadal variability of precipitation over Western North America *J. Clim.* **11** 3148–66

Chowdhury R K and Beecham S 2012 South Australian rainfall—trends and climate drivers Water and climate: policy implementation challenges *Proc. 2nd Practical Responses to Climate Change Conf.* ed K A Daniell (*Canberra, Australia*) (University of Southern Queensland) (available at: https://search.informit.org/documentSummary;dn=891856778041834;res=IELENG;subject=English%20language)

Cionco R G and Pavlov D A 2018 Solar barycentric dynamics from a new solar-planetary ephemeris *Astron. Astrophys.* **615** A153

Cionco R G and Pavlov D 2017 The solar barycentric dynamics from a new solar-planetary ephemeris (available at: pangaea.de/10.1594/PANGAEA.882534?format=html)

Currie R G 1993 Luni-solar 18.6- and 10–11-year solar cycle signals in South African rainfall *Int. J. Climatol.* **13** 237–56

Cziczo D J, Froyd K D, Hoose C, Jensen E J, Diao M, Zondlo M A, Smith J B, Twohy C H and Murphy D M 2013 Clarifying the dominant sources and mechanisms of cirrus cloud formation *Science* **340** 1320–4

DeLong K L, Quinn T M, Taylor F W, Lin K and Shen C-C 2012 Sea surface temperature variability in the southwest tropical Pacific since AD 1649 *Nat. Clim. Change* **2** 799–804

Dhomse S S, Saunders R W, Tian W, Chipperfield M P and Plane J M C 2013 Plutonium-238 observations as a test of modeled transport and surface deposition of meteoric smoke particles *Geophys. Res. Lett.* **40** 4454–8

Ghil M and Vautard R 1991 Interdecadal oscillations and the warming trend in global temperature time series *Nature* **350** 324–7
Hays J D, Imbrie J and Shackleton N J 1976 Variations in the Earth's Orbit: pacemaker of the ice ages *Science* **194** 1121–32
Held I M and Soden B J 2006 Robust responses of the hydrological cycle to global warming *J. Clim.* **19** 5686–99
Hossain I, Rasel H M, Imteaz M A and Mekanik F 2018 Long-term seasonal rainfall forecasting: efficiency of linear modelling technique *Environ. Earth Sci.* **77** 280
Joshi M, Hall R A, Stevens D P and Hawkins E 2023 The modelled climatic response to the 18.6-year lunar nodal cycle and its role in decadal temperature trends *Earth Syst. Dyn.* **14** 443–55
Jouzel J *et al* 2007 Orbital and millennial Antarctic climate variability over the past 800,000 years *Science* **317** 793–6
Keeling C D and Whorf T P 1997 Possible forcing of global temperature by the oceanic tides *Proc. Natl Acad. Sci.* **94** 8321–8
Kirby M, Bark R, Connor J, Qureshi M E and Keyworth S 2014 Sustainable irrigation: how did irrigated agriculture in Australia's Murray–Darling basin adapt in the Millennium Drought? *Agric. Water Manage.* **145** 154–62
L'Ecuyer T S, Hang Y, Matus A V and Wang Z 2019 Reassessing the effect of cloud type on Earth's ENERGY balance in the age of active spaceborne observations. Part I: top of atmosphere and surface *J. Clim.* **32** 6197–217
Latif M and Keenlyside N S 2011 A perspective on decadal climate variability and predictability *Deep Sea Res. II* **58** 1880–94
Le Mouël J-L, Lopes F and Courtillot V 2019 A solar signature in many climate indices *J. Geophys. Res.* **124** 2600–19
Li T, Yu Y, Wang X, Liu X, Mao Q and Yuan Y 2025 A review of aerosol-cloud interactions: mechanisms, climate effects, and observation methods *Atmos. Res.* **325** 108267
Liu Z 2012 Dynamics of interdecadal climate variability: a historical perspective *J. Clim.* **25** 1963–95
Loeb N G *et al* 2020 New generation of climate models track recent unprecedented changes in Earth's radiation budget observed by CERES *Geophys. Res. Lett.* **47** e2019GL086705
Lopes F, Le Mouël J L, Courtillot V and Gibert D 2021 On the shoulders of Laplace *Phys. Earth Planet Inter.* **316** 106693
Lorius C, Jouzel J, Ritz C, Merlivat L, Barkov N I, Korotkevich Y S and Kotlyakov V M 1985 A 150,000-year climatic record from Antarctic ice *Nature* **316** 591–6
Mathews J D, Janches D, Meisel D D and Zhou Q H 2001 The micrometeoroid mass flux into the upper atmosphere: Arecibo results and a comparison with prior estimates *Geophys. Res. Lett.* **28** 1929–32
Morice C P, Kennedy J J, Rayner N A, Winn J P, Hogan E, Killick R E, Dunn R J H, Osborn T J, Jones P D and Simpson I R 2021 An updated assessment of near-surface temperature change from 1850: the HadCRUT5 data set *J. Geophys. Res.* **126** e2019JD032361
Nesvorný D, Jenniskens P, Levison H F, Bottke W F, Vokrouhlický D and Gounelle M 2010 Cometary origin of the zodiacal cloud and carbonaceous micrometeorites. implications for hot debris disks *Astrophys. J.* **713** 816
Ogurtsov M G 2020 Possible contribution of the gravitational influence of Jupiter and Saturn to the 60-year variation in global temperature *Geomagn. Aeron.* **60** 391–5
Ogurtsov M G and Raspopov O M 2011 Possible impact of interplanetary and interstellar dust fluxes on the Earth's climate *Geomagn. Aeron.* **51** 275–83
Ormaza-González F I, Espinoza-Celi M E and Roa-López H M 2022 Did Schwabe cycles 19–24 influence the ENSO events, PDO, and AMO indexes in the Pacific and Atlantic Oceans? *Glob. Planet. Change* **217** 103928
Pedregosa F *et al* 2011 Scikit-learn: machine learning in python *J. Mach. Learn. Res.* **12** 2825–30 (arXiv:1201.0490)
Plane J M C 2012 Cosmic dust in the earth's atmosphere *Chem. Soc. Rev.* **41** 6507–18
Power S and Colman R 2006 Multi-year predictability in a coupled general circulation model *Clim. Dyn.* **26** 247–72
Rayner N A, Parker D E, Horton E B, Folland C K, Alexander L V, Rowell D P, Kent E C and Kaplan A 2003 Global analyses of sea surface temperature, sea ice, and night marine air temperature since the late nineteenth century *J. Geophys. Res.* **108** 2002JD002670
Rojas J, Duprat J, Engrand C, Dartois E, Delauche L, Godard M, Gounelle M, Carrillo-Sánchez J D, Pokorný P and Plane J M C 2021 The micrometeorite flux at Dome C (Antarctica), monitoring the accretion of extraterrestrial dust on Earth *Earth Planet. Sci. Lett.* **560** 116794
Sarachik E S and Cane V A 2010. The El Niño-Southern oscillation phenomenon (Cambridge University Press) (available at: www.cambridge.org/core/books/el-ninosouthern-oscillation-phenomenon/DBB063CB79D4E97350B09F16B8A156A1)
Scafetta N 2010 Empirical evidence for a celestial origin of the climate oscillations and its implications *J. Atmos. Sol. Terr. Phys.* **72** 951–70
Scafetta N 2014a Multi-scale dynamical analysis (MSDA) of sea level records versus PDO, AMO, and NAO indexes *Clim. Dyn.* **43** 175–92
Scafetta N 2014b The complex planetary synchronization structure of the solar system *Pattern Recognit. Phys.* **2** 1–19
Scafetta N, Milani F and Bianchini A 2020 A 60-year cycle in the meteorite fall frequency suggests a possible interplanetary dust forcing of the Earth's climate driven by planetary oscillations *Geophys. Res. Lett.* **47** e2020GL089954
Schneider J *et al* 2021 Aircraft-based observation of meteoric material in lower-stratospheric aerosol particles between 15 and 68° N *Atmos. Chem. Phys.* **21** 989–1013
Schneider U, Hänsel S, Finger P, Rustemeier E and Ziese M 2022 GPCC full data monthly version 2022 at 2.5°: monthly land-surface precipitation from rain-gauges built on GTS-based and historic data: globally gridded monthly totals, [data set] min. 20 MB-max. 300 MB per gzip archive (10 years per archive) (available at: https://opendata.dwd.de/climate_environment/GPCC/html/fulldata-monthly_v2022_doi_download.html)
Selkirk T F, Western A W and Webb J A 2025a Interdecadal cycles in Australian annual rainfall *Hydrol. Earth Syst. Sci.* **29** 2167–84
Selkirk T F, Western A W and Webb J A 2025b Interdecadal rainfall cycles in spatially coherent global regions and their relationship to the climate modes *Hydrol. Earth Syst. Sci.* **29** 5737–54
Slivinski L C *et al* 2019 Towards a more reliable historical reanalysis: improvements for version 3 of the twentieth century reanalysis system *Q. J. R. Meteorol. Soc.* **145** 2876–908
Wang W and McPhaden M J 2000 The surface-layer heat balance in the equatorial Pacific Ocean. Part II: interannual variability *J. Phys. Oceanogr.* **30** 2989–3008
Wild M, Ohmura A, Schär C, Müller G, Folini D, Schwarz M, Hakuba M Z and Sanchez-Lorenzo A 2017 The global energy balance archive (GEBA) version 2017: a database for worldwide measured surface energy fluxes *Earth Syst. Sci. Data* **9** 601–13
Williams A P, Anchukaitis K J, Woodhouse C A, Meko D M, Cook B I, Bolles K and Cook E R 2021 Tree rings and observations suggest no stable cycles in Sierra Nevada cool-season precipitation *Water Resour. Res.* **57** e2020WR028599
Yasuda I 2018 Impact of the astronomical lunar 18.6-yr tidal cycle on El-Niño and southern oscillation *Sci. Rep.* **8** 15206